JACS
JOURNAL OF THE AMERICAN CHEMICAL SOCIETY

Communication

pubs.acs.org/JACS

Defect-Dominated Shape Recovery of Nanocrystals: A New Strategy for Trimetallic Catalysts

Yuen Wu,[†] Dingsheng Wang,[†] Xiaobin Chen,[§] Gang Zhou,[∥] Rong Yu,[‡] and Yadong Li*,[†]

[†]Department of Chemistry, [‡]Beijing National Center for Electron Microscopy, Department of Materials Science and Engineering, and [§]Department of Physics, Tsinghua University, Beijing 100084, China

[∥]State Key Laboratory of Chemical Resource Engineering, Beijing University of Chemical Technology, Beijing 100029, China

Supporting Information

ABSTRACT: Here we present a shape recovery phenomenon of Pt−Ni bimetallic nanocrystals that is unequivocally attributed to the defect effects. High-resolution electron microscopy revealed the overall process of conversion from concave octahedral Pt_3Ni to regular octahedral Pt_3Ni@Ni upon Ni deposition. Further experiments and theoretical investigations indicated that the intrinsic defect-dominated growth mechanism allows the site-selective nucleation of a third metal around the defects to achieve the sophisticated design of trimetallic Pt_3Ni@M core−shell structures (M = Au, Ag, Cu, Rh). Consideration of geometrical and electronic effects indicated that trimetallic atomic steps in Pt_3Ni@M could serve as reactive sites to significantly improve the catalytic performance, and this was corroborated by several model reactions. The synthesis strategy based on our work paves the way for the atomic-level design of trimetallic catalysts.

Noble metals are of immense importance in diverse areas such as chemical industry,[1] new energy resources,[2] and gas sensors.[3] The properties of noble metals for use in heterogeneous catalysis are strongly dependent on their surface atomic arrangement.[4] Because of their predominant role in actual catalytic processes, defects on the noble metal surface (e.g., steps, kinks, and edges) have stimulated extensive investigations.[5,6] These open structures, which have a high density of low-coordinate atoms, usually favor reducing the activation energy for structure-sensitive reactions.[7] For example, some typical reports have pointed out that the cleavage or formation of molecular π bonds preferentially occurs on unsaturated coordinated surface atoms.[8] Notably, recent progress in computational catalysis, surface science, and nanotechnology has significantly enhanced our understanding that the catalytic characteristics are dependent not only on geometrical effects but also electronic effects.[9]

The interface perimeter of a hybrid structure (e.g., metal−oxide or metal−metal) has generally been viewed as the most active site for some model reactions (e.g., low-temperature CO oxidation,[10] water-gas shift reaction,[11] etc.). Furthermore, the incorporation of a third metal into bimetallic structures to form ternary metallic nanocrystals (NCs) has been shown to improve thecatalytic activity toward the methanol electro-oxidation reaction by varying the adsorption energy and the ease of charge transfer.[12] Encouraged by this progress, the design of multicenter and multifunctional nanostructures to optimize the catalytic performance is currently becoming one promising area. In view of the different rates of nucleation and growth, traditional synthetic methodologies such as coreduction and thermal decomposition are becoming insufficient to completely control the size, composition, and morphology of trimetallic nanostructures.[13] In general, defect zones of NCs are more susceptible to attack by active species such as etchants and/or newly formed nuclei.[14] Sophisticated use of the volatility of defects in crystal growth allows the third metal to be introduced and site-selectively anchored around the defects to modify the surface electronic structure. However, surface defects, which usually serve as active sites for catalysis, normally vanish faster during the growth stage and thus are preferentially eliminated on the final surface.[15] Therefore, in the context of defect survival, precise manipulation of the growth of the third metal at the atomic level to achieve the optimal tradeoff of geometrical and electronic effects is very challenging.

Through selective etching of the more active metal and rearrangement of the remaining metal atoms, we recently demonstrated that chemical etching can be utilized as an effective strategy to excavate surfaces of bimetallic NCs and thus generate defects.[16] Transmission electron microscopy (TEM) (Figure 1a) and spherical aberration (SA)-corrected high-resolution TEM (HRTEM) [Figure S1 in the Supporting Information (SI)] images indicated the transformation from octahedral $PtNi_3$ alloy NCs to concave Pt_3Ni alloy NCs, whose surfaces possess a high density of low-coordinate atoms situated at concave atomic steps (ASs). In the second procedure, concave Pt_3Ni seeds were redispersed in a Ni^{2+}-rich chemical environment and underwent a solvothermal process. From a thermodynamic point of view, the γ{111} facets have the lowest surface energy.[17] As expected, octahedral NCs were reborn after the seeded growth process of Ni (Figure 1b). Additional HRTEM images (Figure 1c) showed that the regained octahedrons were bounded by eight well-defined {111} facets. To specify the microstructure of the regained octahedrons, we carried out elemental mapping measurements. For the original Pt_3Ni seeds, both Pt and Ni were evenly distributed in each nanoparticle (Figure 1d), indicating the alloyed phase of concave Pt_3Ni. Quite strikingly, in the as-obtained octahedral NCs, Pt exhibited a hexapod-like distribution as in the initial concave seeds, whereas for Ni a relatively octahedral distribution was observed (Figure 1e). Thus, the core of concave Pt_3Ni may be coated with a shell of Ni

Received: July 10, 2013
Published: August 5, 2013

dx.doi.org/10.1021/ja4068063 | J. Am. Chem. Soc. 2013, 135, 12220−12223

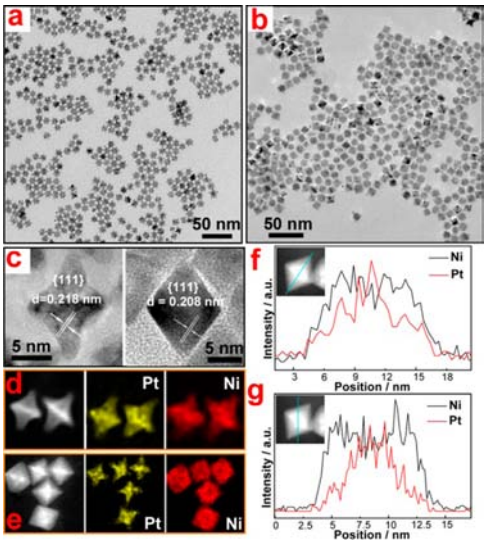

Figure 1. (a, b) TEM images of (a) concave Pt_3Ni NCs and (b) Pt_3Ni@Ni core–shell NCs. (c) HRTEM images of concave (left) Pt_3Ni and (right) Pt_3Ni@Ni core–shell NCs. (d, e) Elemental maps of (d) concave Pt_3Ni and (e) Pt_3Ni@Ni core–shell NCs. (f, g) Cross-sectional compositional line profiles of a Pt_3Ni@Ni core–shell octahedron.

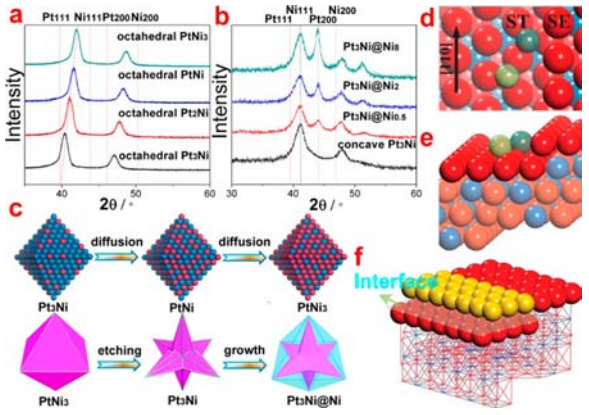

Figure 2. (a, b) XRD patterns representing the phase evolutions (a) from octahedral Pt_3Ni alloy seeds to octahedral $PtNi_3$ alloy NCs and (b) from concave $PtNi_3$ alloy seeds to octahedral Pt_3Ni@Ni core–shell NCs. (c) Schematic illustrations of the two different seeded growth processes. (d, e) Atomic structures of the {111} step of concave Pt_3Ni nanocrystals: (d) top view; (e) side view. The labels SE and ST indicate the step edge and step terrace, respectively. The dark-green and light-green balls show Ni atoms located at the SE and ST binding sites as described in the text. Blue, red, and pink balls represent Ni, surface Pt, and nonsurface Pt atoms, respectively. (f) Interface between M atoms and concave Pt_3Ni nanocrystals during shape recovery. Red, blue, and yellow balls/lattice sites represent Pt, Ni and M atoms, respectively.

after the seeded growth process. The cross-sectional compositional line profiles of Pt_3Ni@Ni oriented along different directions also corroborated this unconventional core–shell architecture (Figure 1f,g).

For comparison, we also used regular octahedral Pt_3Ni NCs as the seeds for the second growth of Ni and observed an uneventful shape evolution (i.e., only size enlargement; Figure S2). X-ray diffraction (XRD) has proven to be a facile and versatile technique to capture the internal crystal structure changes during the seeded growth process. For only size-enlarged octahedral NCs, the peak positions gradually shifted to higher 2θ values relative to those of the initial octahedral Pt_3Ni NCs as a result of the decreased lattice spacing (Figure 2a). According to the diffusion-dominated growth mechanism,[18] since the octahedral seeds were unifaceted with eight most stable {111} faces for face-centered-cubic (fcc) structures, the smaller Ni atoms would diffuse inside and the Pt atoms would rearrange in the bimetallic lattice, resulting in the phase transformation from alloyed Pt_3Ni to alloyed $PtNi_3$ (Figure 2c top). Clearly, the situation was completely different when concave Pt_3Ni NCs were used as seeds for the second growth of Ni. The well-defined XRD peaks corresponding to alloyed Pt_3Ni remained unchanged (Figure 2b), while new emerging peaks could be indexed to fcc nickel grown on concave Pt_3Ni. This unequivocally confirmed the synthesis of the Pt_3Ni@Ni core–shell structure with an alloyed Pt_3Ni core and Ni shell (Figure 2c bottom).

To elucidate the physical origin of shape recovery and further corroborate the beneficial effects of defects on the shape- and composition-controlled synthesis of multimetallic NCs, we performed extensive theoretical investigations of the underlying growth mechanism using density functional theory (DFT). The most prominent characteristic of the concave Pt_3Ni NCs is that they are fully covered with numerous Pt-segregated ASs instead of eight {111} faces as in the octahedral NCs. All of the ASs have two kinds of surface atoms, step edge (SE) and step terrace (ST), leading to two different binding sites (Figure 2d,e). The stable binding of fresh Ni atoms to the ASs initiates the shape recovery. To this end, we first compared the stabilities of Ni atoms located at the different sites on the {111} ASs. Our DFT calculations indicated that Ni atoms prefer the SE sites, where they are coordinated by two SE Pt atoms and three ST Pt atoms, over the threefold hollow ST sites, where they are coordinated by only three ST atoms (Figure 2d,e and Table S1 in the SI). The edge-dependent Ni deposition can be viewed as the continuous advance of Ni ASs on the (111) surface. In this manner, we can affirm that the shape recovery follows a distinctive "step-induced/terrace-assisted" growth mechanism. Further generalizing to other metals akin to Ni, we found that the growth of M (M = Au, Ag, Cu, Rh, Fe) proceeds by "step-induced/terrace-assisted" growth mechanism. More precisely, the step-induced behavior occurs regardless of the crystal structure and lattice parameter of M (Table S1) because of its growth along the [110] direction, aligned with the {111} SE of the Pt_3Ni NCs (Figure 2d). However, the subsequent terrace-assisted growth is strongly dependent on the structural and electronic properties of M relative to Pt as the interface forms (Figure 2f). Similar to Pt-based solid solution counterparts, the Pt_3Ni–M interface effects were expected to be small for M = Au, Ag, Cu, Rh, and Ni because they have the same crystal structure (fcc) and only small differences in electron distribution at the interface.[19] In contrast, for M = Fe, which has a body-centered-cubic (bcc) structure and a significantly different electron distribution due in large part to its different coordination environment, the deformation induced by the lattice mismatch [bcc(110) vs fcc(111)] at the interface should result in a higher interface energy,[20] which should hamper the recovery growth.

To reinforce the above inferences, we further carried out the consistent synthesis of trimetallic NCs based on concave Pt_3Ni. Figure 3 summarizes the growth process of Au on concave Pt_3Ni as an example. By controlling the amount of chloroauric acid, we obtained a series of Pt_3Ni@Au trimetallic core–shell structures with different degrees of concavity and surface Au coverages (Figure S3). This success is of great significance for achieving shape and composition control of multimetallic NCs with perfect

dx.doi.org/10.1021/ja4068063 | J. Am. Chem. Soc. 2013, 135, 12220–12223

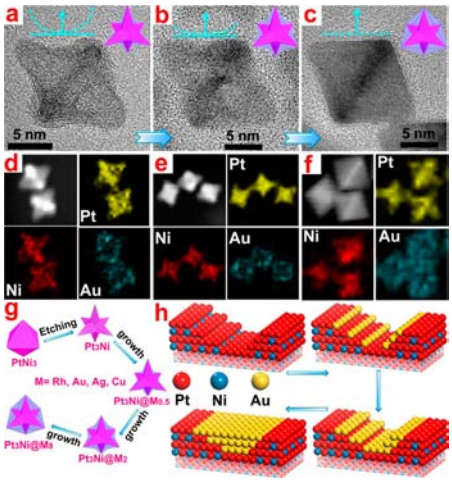

Figure 3. (a–c) SA-corrected HRTEM images of (a) $Pt_3Ni@Au_{0.5}$, (b) $Pt_3Ni@Au_2$, and (c) $Pt_3Ni@Au_8$. (d–f) Elemental maps of (d) $Pt_3Ni@Au_{0.5}$, (e) $Pt_3Ni@Au_2$, and (f) $Pt_3Ni@Au_8$. (g) Schematic illustration of the evolution from octahedral $PtNi_3$ to $Pt_3Ni@M_8$ (M = Rh, Au, Ag, Cu). (h) Schematic illustration of the growth of Au on the Pt surface.

monodispersity. Consistent with our theoretical predictions, the atoms of surface defects would first hold the Au atoms or clusters. The SA-corrected HRTEM image of $Pt_3Ni@Au_{0.5}$ in Figure 3a shows that the atomic steps remained omnipresent after trace deposition of Au and that the concave morphology was still predominant for the products. With much more Au present, the Pt atomic steps gradually vanished, and the newly generated Au steps served as new selective-deposition sites (Figure 3b). Finally, this type of site-specific growth in which the Au atoms were only confined around the defects was finished when the perfect {111} faces were repaired, generating the octahedrons (Figure 3c). Elemental mapping was also employed to track this Au growth process (Figure 3d–f). The concave octahedron-like distributions of Pt and Ni continuously remained the same as in the original stage. For Au, a cruciform area with darker contrast was conspicuously visible in the middle of the NCs, evidencing a saddle-shaped distribution. In the XRD pattern (Figure S4), a set of peaks assigned to Au gradually emerged beside the peaks belonging to Pt_3Ni alloy as the growth proceeded. X-ray photoelectron spectroscopy (XPS) showed an elevated surface atomic ratio of Au, also testifying to the segregation of Au on the surface (Table S2). The combination of HRTEM, elemental mapping, XRD, and XPS confirmed that the Au was preferentially added to the concave region during growth, finally leading to these unique trimetallic core–shell structures.

Two control experiments were subsequently conducted to further understand the critical role of defects. First, the use of more Au precursor did not result in bigger octahedrons but gave mixed morphologies (Figure S5), indicating that the defects are pivotal to avoid self-nucleation and achieve the thermodynamically controlled growth pathway. Second, a one-pot synthesis using the Pt, Ni, and Au salts as precursors under the similar conditions but without the concave Pt_3Ni seeds afforded only alloyed Pt–Ni–Au NPs with irregular shapes instead of the specific octahedral core–shell structure (Figure S6). In good agreement with aforementioned theoretical model, this shape recovery process was found to be dependent at some level on the crystal structure of the third metal. Figure S7 clearly shows that the seeded growth of iron with its bcc structure did not lead to the octahedral $Pt_3Ni@Fe$ structure. Actually, this defect-dominated effect was readily generalized to the synthesis of other types of trimetallic core–shell structures, such as $Pt_3Ni@Ag$, $Pt_3Ni@Cu$, and $Pt_3Ni@Rh$ (Figures S8–S10), for which both the crystal structure and atomic size of M follow the principles confirmed by our DFT calculations. All of these trimetallic structures were further verified by XRD and energy-dispersive spectroscopy (EDS) measurements (Figure S11). For the sake of understanding, the evolution from octahedral $PtNi_3$ to $Pt_3Ni@M$ and the fine growth of Au on Pt ASs are schematically illustrated in Figure 3g,h, respectively.

By sophisticated decoration with the third metal, the geometrical and electronic effects of the NCs could be fine-tuned to optimize the catalytic activity and selectivity. To the best of our knowledge, Au(0) is inert with respect to activation of C–X bonds (X = Cl, Br, I).[21] According to the rendered mechanism, we could hypothesize that Pt(0) is the active state for the Suzuki–Miyaura reaction: the valence state of Pt would increase in the oxidative addition process and decrease to Pt(0) in the subsequent reductive elimination. The $Pt_3Ni@Au_{0.5}$ catalyst exhibited an exceptionally higher catalytic activity than Pt_3Ni (Figure 4a), probably because of the presence of trace Au on the surface, which may facilitate the reduction of Pt(II) to Pt(0). Surprisingly, trimetallic catalysts with increasing quantities of Au exhibited a significant decay of activity, which may result because the excess Au blocks the exposed Pt sites, breaking the interaction with substrate.

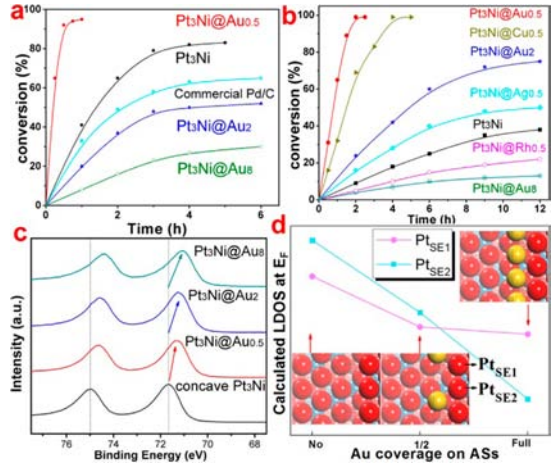

Figure 4. Conversion as a function of time in (a) the Suzuki–Miyaura reaction and (b) reduction of nitrobenzene using formic acid as a hydrogen source catalyzed by trimetallic catalysts containing 0.5 atom % Pt. (c) High-resolution Pt 4f XPS scans for the initial concave octahedral $PtNi_3$ and trimetallic $Pt_3Ni@Au$ NCs. (d) DFT-calculated local densities of states (LDOS) at the Fermi energy (E_F) for Pt_{SE1} and Pt_{SE2} atoms as functions of the Au coverage at the atomic steps. The atomic structures are shown in the insets. Red, blue, and yellow balls respresent Pt, Ni, and Au atoms, respectively.

Thanks to recent progress in catalysis of dehydrogenation reactions of formic acid (FA), which is one of the major products in biomass processing, FA can be used as a safe and convenient hydrogen carrier for energy applications.[22] H_2 is released via the catalytic dehydrogenation reaction $HCOOH \rightarrow H_2 + CO_2$ but is usually accompanied by low levels of CO produced by the undesired dehydration reaction $HCOOH \rightarrow H_2O + CO$. Utilizing the stoichiometric hydrogenation of nitrobenzene to aniline, we established a tandem reaction involving decomposition of FA followed by reduction and evaluated the activity

dx.doi.org/10.1021/ja4068063 | J. Am. Chem. Soc. 2013, 135, 12220–12223

and selectivity. Among the as-prepared trimetallic multifunctional catalysts, $Pt_3Ni@Au_{0.5}$ (containing 0.5 atom % Pt) exhibited the best performance with respect to both activity and selectivity, and a similar deactivation trend was also tracked when too much Au was grown on the surface of the concave Pt_3Ni seeds (Figure 4b). Thus, the existence of atomic steps composed of Pt and Au play a crucial role in the catalytic behavior. It is noteworthy that the decorated element that optimizes the catalytic performance is dependent on the specific reaction. As another comparable important industrial example, the oxidation of benzyl alcohol to carbonyl compounds is a pivotal process in chemical industry.[23] In this context, $Pt_3Ni@Ag_{0.5}$ achieved the best catalytic performance for the selective oxidation of benzyl alcohol to benzaldehyde (Table S5).

To gain insight into the structure−activity relationships of trimetallic NCs, as evidenced by the maximum catalytic activity at $Pt_3Ni@Au_{0.5}$, we studied the electronic properties of $Pt_3Ni@Au$ as a function of the Au coverage from both the experimental and theoretical perspective. Very recently, electronic coupling between the hybrid structures has been reported, indicating that electrons can be transferred from the Au domains to Pt.[24] In this work, XPS was also utilized to analyze the electron transfer process. An apparent shift of the Pt $4f_{7/2}$ and $4f_{5/2}$ peaks to lower binding energy was detected for $Pt_3Ni@Au$ relative to concave Pt_3Ni (Figure 4c). These results positively demonstrated that the Au domains may donate electrons to Pt, thereby reducing oxidized Pt(II) in actual reactions. Comparatively, similar and opposite shifts were also observed for the Ni and Au XPS peaks, respectively (Figure S13). On the other hand, our DFT calculations clearly indicated that the deposition of Au on the step reduces the local density of states (LDOS) at the Fermi energy (E_F) for Pt atoms at the ASs as a result of the d^{10} electron configuration of Au (Figure 4d). According to the Anderson−Newns model for adsorbate−metal bonding,[25] such a decrease means that Au-deposited Pt ASs have fewer electronic states to respond to the adsorbate, decreasing their ability to facilitate the hybridization process between the adsorbate and the NC. It is expected that these two opposite contributions, which monotonically vary with Au coverage, would make mixed Au−Pt ASs possess the possibly highest catalytic performance. This is consistent with the experimental results (Figure 4a). Moreover, alternate structural arrangements of Au and Pt at the SE would to a certain extent improve the reaction selectivity from the viewpoint of the control of reactive sites. That is to say, the introduction of the M may shed light on the design of novel materials with simultaneous enhancement in both activity and selectivity for catalytic applications. In particular, the unique growth mechanism confirmed here, which involves the step-induced M deposition associated only with Pt ASs, allows most metals to form various M−Pt ASs for some special reactions.

In summary, we have discovered a novel shape recovery phenomenon of NCs that is dominated by the defects. On the basis of the rendered "step-induced/terrace-assisted" growth mechanism, we unequivocally confirmed two requirements for the synthesis of a new trimetallic or multimetallic core@shell structure by shape recovery: (1) the same crystal structure and (2) similar atomic radius. Remarkably, the catalytic performance can be significantly improved by sophisticated decoration with the third metal. We foresee that this method will greatly expand our opportunities for rational design of nanocrystal catalysts in the form of fine-tuned geometric and electronic structures.

■ ASSOCIATED CONTENT

Supporting Information

Procedures and additional data. This material is available free of charge via the Internet at http://pubs.acs.org.

■ AUTHOR INFORMATION

Corresponding Author

ydli@mail.tsinghua.edu.cn

Notes

The authors declare no competing financial interest.

■ ACKNOWLEDGMENTS

This work was supported by the State Key Project of Fundamental Research for Nanoscience and Nanotechnology (2011CB932401, 2011CBA00500), the National Key Basic Research Program (2012CB224802), and the National Natural Science Foundation (21221062, 21171105, 21131004) and used resources of the Beijing National Center for Electron Microscopy.

■ REFERENCES

(1) Hong, J. W.; Kang, S. W.; Choi, B.-S.; Kim, D.; Lee, S. B.; Han, S. W. *ACS Nano* **2012**, *6*, 2410.
(2) Guo, S.; Wang, E. *Nano Today* **2011**, *6*, 240.
(3) Gao, C.; Lu, Z.; Liu, Y.; Zhang, Q.; Chi, M.; Cheng, Q.; Yin, Y. *Angew. Chem., Int. Ed.* **2012**, *51*, 5629.
(4) Zhou, K.; Li, Y. *Angew. Chem., Int. Ed.* **2012**, *51*, 602.
(5) Quan, Z.; Wang, Y.; Fang, J. *Acc. Chem. Res.* **2013**, *46*, 191.
(6) Zhang, L.; Niu, W.; Xu, G. *Nano Today* **2012**, *7*, 586.
(7) Dahl, S.; Logadottir, A.; Egeberg, R.; Nielsen, J. H.; Chorkendorff, I.; Törnqvist, E.; Nørskov, J. K. *Phys. Rev. Lett.* **1999**, *83*, 1814.
(8) Liu, Z.-P.; Hu, P. *J. Am. Chem. Soc.* **2003**, *125*, 1958.
(9) Stamenkovic, V.; Mun, B. S.; Mayrhofer, K. J. J.; Ross, P. N.; Markovic, N. M.; Rossmeisl, J.; Greeley, J.; Nørskov, J. K. *Angew. Chem., Int. Ed.* **2006**, *45*, 2897.
(10) Ta, N.; Liu, J.; Chenna, S.; Crozier, P. A.; Li, Y.; Chen, A.; Shen, W. *J. Am. Chem. Soc.* **2012**, *134*, 20585.
(11) Rodriguez, J.; Ma, S.; Liu, P.; Hrbek, J.; Evans, J.; Perez, M. *Science* **2007**, *318*, 1757.
(12) Wang, D. Y.; Chou, H. L.; Lin, Y. C.; Lai, F. J.; Chen, C. H.; Lee, J. F.; Hwang, B. J.; Chen, C. C. *J. Am. Chem. Soc.* **2012**, *134*, 10011.
(13) Wanjala, B. N.; Fang, B.; Luo, J.; Chen, Y.; Yin, J.; Engelhard, M. H.; Loukrakpam, R.; Zhong, C. J. *J. Am. Chem. Soc.* **2011**, *133*, 12714.
(14) Xia, Y.; Xiong, Y.; Lim, B.; Skrabalak, S. E. *Angew. Chem., Int. Ed.* **2009**, *48*, 60.
(15) Zhou, Z. Y.; Tian, N.; Li, J. T.; Broadwell, I.; Sun, S. G. *Chem. Soc. Rev.* **2011**, *40*, 4167.
(16) Wu, Y.; Wang, D.; Niu, Z.; Chen, P.; Zhou, G.; Li, Y. *Angew. Chem.* **2012**, *124*, 12692.
(17) Wang, Z. *J. Phys. Chem. B* **2000**, *104*, 1153.
(18) Chen, W.; Yu, R.; Li, L.; Wang, A.; Peng, Q.; Li, Y. *Angew. Chem., Int. Ed.* **2010**, *49*, 2917.
(19) de Boer, F. R.; Boom, R.; Mattens, W. C. M.; Miedema, A. R.; Niessen, A. K. *Cohesion in Metals: Transition Metal Alloys*; Elsevier: Amsterdam, 1988; p 758.
(20) Somoza, J.; Gallego, L.; Rey, C.; Fernandez, H.; Alonso, J. *Philos. Mag. B* **1992**, *65*, 989.
(21) Wegner, H. A.; Auzias, M. *Angew. Chem., Int. Ed.* **2011**, *50*, 8236.
(22) Zhang, S.; Metin, O.; Su, D.; Sun, S. *Angew. Chem., Int. Ed.* **2013**, *52*, 3681.
(23) Mallat, T.; Baiker, A. *Chem. Rev.* **2004**, *104*, 3037.
(24) Yang, J.; Ying, J. Y. *Angew. Chem., Int. Ed.* **2011**, *50*, 4637.
(25) Newns, D. *Phys. Rev.* **1969**, *178*, 1123.